International Journal of Minerals, Metallurgy and Materials
Volume 25, Number 10, October 2018, Page 1156
http://doi.org/10.1007/s12613-018-1667-7

Effects of aluminum and titanium on the microstructure of ODS steels fabricated by hot pressing

Qian Zhao, Li-ming Yu, Yong-chang Liu, Yuan Huang, Zong-qing Ma, and Hui-jun Li

State Key Lab of Hydraulic Engineering Simulation and Safety, School of Materials Science & Engineering, Tianjin University, Tianjin 300354, China
(Received: 30 January 2018; revised: 5 March 2018; accepted: 6 March 2018)

Abstract: Three oxide-dispersion-strengthened (ODS) steels with compositions of Fe–14Cr–2W–0.2V–0.07Ta–0.3Y_2O_3 (wt%, so as the follows) (14Y), Fe–14Cr–2W–0.2V–0.07Ta–1Al–0.3Y_2O_3 (14YAl), and Fe–14Cr–2W–0.2V–0.07Ta–0.3Ti–0.3 Y_2O_3 (14YTi) were fabricated by hot pressing. Transmission electron microscopy (TEM) was used to characterize the microstructures and nanoparticles of these ODS steels. According to the TEM results, 14Y, 14YAl, and 14YTi ODS steels present similar bimodal structures containing both large and small grains. The addition of Al or Ti has no obvious effect on the microstructure of the steels. The spatial and size distribution of the nanoparticles was also analyzed. The results indicate that the average size of nanoparticles in the 14YTi ODS steel is smaller than that in the 14YAl ODS steel. Nanoparticles such as Y_2O_3, $Y_3Al_5O_{12}$ and $YAlO_3$, and $Y_2Ti_2O_7$ were identified in the 14Y, 14YAl, and 14YTi ODS steels, respectively.

Keywords: hot pressing; ODS steel; mechanical alloying; bimodal structure; nanoparticle; aluminum; titanium

1. Introduction

The development of nuclear reactors has been an urgent issue for several decades as the demand for energy has increased. In the evolution of nuclear reactors, the structural materials have posed a key problem that influences the overall reactor performance [1–3]. Currently, oxide-dispersion-strengthened (ODS) steels are considered promising candidates for fourth-generation nuclear systems because of their good resistance to irradiation-induced embrittlement and void swelling and their excellent high-temperature mechanical properties [4–6]. These outstanding performance characteristics of ODS steels are ascribed to the existence of stable nanoparticles. These oxide particles hinder grain-boundary migration and dislocation slipping, thereby stabilizing the microstructure in a severe service environment [7–10]. ODS steels are generally fabricated by mechanical alloying and subsequent consolidation at high temperature. During the mechanical alloying process, the as-mixed powders undergo plastic deformation, fracture, and cold welding, which can effectively reduce the grain size of the as-mixed powders [11–14]. After the consolidation process, the as-milled powders sinter together and a dense sample is obtained. Several consolidation techniques for ODS steels have been investigated, including hot pressing (HP), hot extrusion, hot isostatic pressing, and spark plasma sintering (SPS) [7,15–18].

The composition of the as-mixed powders can be controlled by adding other elements via mechanical alloying. In ODS steels, Y_2O_3 particles are the initial strengthening phases that function as the obstacles to grain growth [19–20]. To improve the strengthening effect of nanoparticles, alloying elements such as Al and Ti have been introduced into the as-mixed powders to fabricate ODS steels strengthened by Y–Al–O and Y–Ti–O particles [21–26]. A recent study has shown that the addition of Al to ferritic ODS steels can increase their corrosion resistance by forming compact Al_2O_3 scales with enhanced adherence to the metal substrate [27]. Also, Al plays the dominant role in improving the isotropy during tensile tests and decreasing the 475°C brittleness in Fe–Cr alloys [28–29]. The addition of Ti enhances the mechanical performance of ODS steels by leading to the formation of Y–Ti–O particles that can effectively refine the microstructure. The ODS steels containing Ti have also been demonstrated to be more resistant to coarsening than those without Ti [30]. The combined effect of Al and Ti on the microstructures and mechanical properties of ODS steels

Corresponding authors: Li-ming Yu E-mail: lmyu@tju.edu.cn; Yong-chang Liu E-mail: ycliu@tju.edu.cn

has been adequately developed, while knowledge of the influences of single Al or Ti on the microstructures of ODS steels is insufficient.

In the present work, Y_2O_3 powders were added to pre-alloyed powders to prepare ODS steels without other alloying elements. For comparison, Al and Ti powders were added to pre-alloyed powders, along with Y_2O_3. The relative densities and Vickers hardness of these three ODS steels were measured and analyzed. Microstructure differences and the spatial dispersion of the oxide particles were characterized by transmission electron microscopy (TEM). The size distributions of the oxide particles in the ODS samples were also investigated by TEM. As the sinking sites for defects, nanoparticles in the ODS steels were identified on the basis of high-resolution transmission electron microscopy (HRTEM) images.

2. Experimental

The pre-alloyed Fe–14Cr–2W–0.2V–0.07Ta (wt%) powders were obtained via a gas atomization process, and the Y_2O_3, Al, and Ti powders were mixed with the pre-alloyed powders to produce three types of ODS samples with compositions of Fe–14Cr–2W–0.2V–0.07Ta–$0.3Y_2O_3$ (14Y), Fe–14Cr–2W–0.2V–0.07Ta–1Al–$0.3Y_2O_3$ (14YAl), and Fe–14Cr–2W–0.2V–0.07Ta–0.3Ti–$0.3Y_2O_3$ (14YTi) by mechanical alloying. Mechanical alloying was performed in a planetary ball mill (QM-3SP4, Nanjing NanDa Instrument Plant, China) for 30 h with the speed of 400 r/min, and the ball-to-powder mass ratio was 15:1. All of the powders were handled and the milling processes were conducted under a high-purity argon atmosphere. The powders obtained by mechanical alloying were then consolidated by HP at 1100°C for 1 h under 60 MPa.

The densities of ODS samples were measured according to Archimedes' principle using an electronic density balance, and the relative densities were calculated on the basis of the theoretical and measured densities. Vickers hardness measurements were performed using a sclerometer with a load of 50 g. Microstructures of the as hot-pressed (as-HPed) samples were observed by TEM. The dispersion, identification, and size distribution of the nanoparticles in the ODS samples were analyzed according to their TEM results. Specimens for TEM were fabricated from 300-μm-thick slices cut from the as-HPed samples. These slices were mechanically thinned and punched into 3-mm-diameter discs, and the discs were subsequently subjected to double-jet electropolishing with a solution of 5vol% perchloric acid and 95vol% ethanol at −20°C.

3. Results and discussion

3.1. Microstructure

Scanning electron microscopy (SEM) images of the pre-alloyed powders and the milled powders are presented in Fig. 1. Fig. 1(a) shows the spherical morphology of the pre-alloyed powders. The average particle size of the pre-alloyed powders is approximately 105 μm. Figs. 1(b)–1(d)

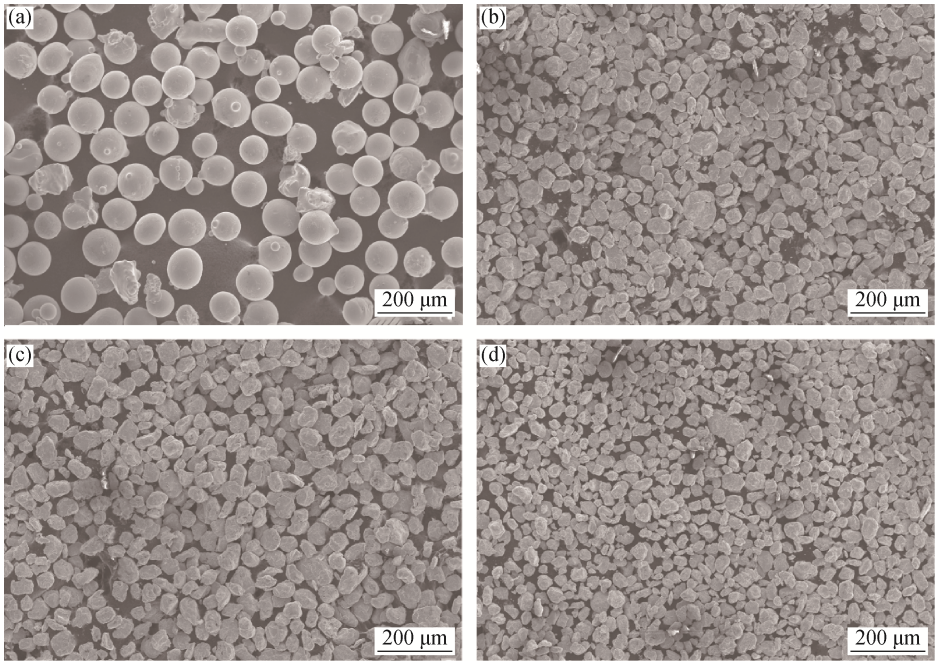

Fig. 1. SEM images of the pre-alloyed powders and the milled powders: (a) pre-alloyed powders; (b) 14Y; (c) 14YAl; (d) 14YTi.

depict the SEM images of 14Y, 14YAl, and 14YTi powders, respectively. The particle size of the milled powders is obviously smaller than that of the pre-alloyed powders, and the 14Y, 14YAl, and 14YTi powders exhibit similar morphologies. The average particle size of 14YAl powders is slightly larger than that of 14Y and 14YTi powders, which is related to their different compositions. The hardness of Al is much lower than that of Ti and Y_2O_3. The addition of Al would weaken the effect of impacts between the grinding balls and the particles, thereby hindering the refinement of particles during mechanical alloying to some extent. The 14Y and 14YTi powders without Al addition would be effectively refined during the mechanical alloying process.

Fig. 2 illustrates the XRD patterns of the consolidated 14Y, 14YAl, and 14YTi ODS steels. No differences are evident from the XRD results. The XRD patterns of the ODS steels show the same peaks of Fe–Cr, meaning that these ODS steels have the same matrix. The microstructures of the ODS samples are shown in Fig. 3. All of the ODS samples possess the same ferritic matrix.

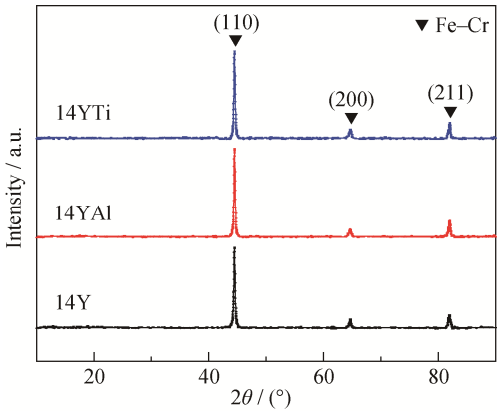

Fig. 2. XRD patterns of the ODS steels.

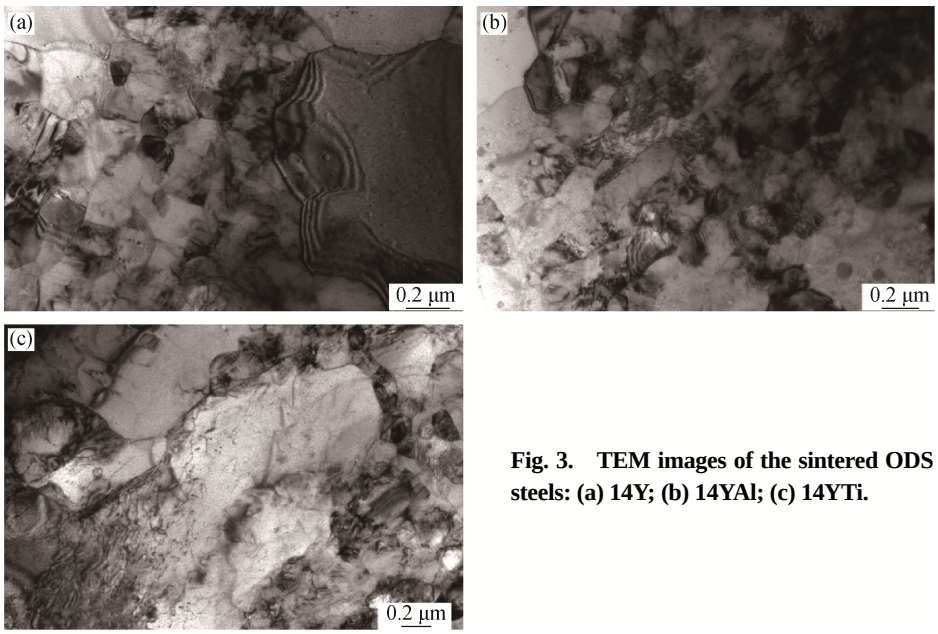

Fig. 3. TEM images of the sintered ODS steels: (a) 14Y; (b) 14YAl; (c) 14YTi.

Fig. 3(a) illustrates the typical microstructure of the 14Y sample. Both small and large grains exist in the sample, and all of the grains show the same equiaxed morphology. The sizes of the small grains are approximately 100–300 nm, whereas the large grains appear to be several microns in size. This bimodal structure results from the disparity in grain size of the pre-alloyed powders and the local inhomogeneity phenomenon during mechanical alloying. The mechanical alloying process can not only reduce the overall grain size of the as-mixed powders but also influence the distribution of the added Y_2O_3, Al, and Ti powders to some extent [12–13]. The inhomogeneous distribution of nanoparticles is one of the factors that leads to the bimodal structure. The different grain sizes and distributions of the added elements would then result in a microstructure with both small and large grains. Fig. 3(b) illustrates the microstructure of the 14YAl ODS sample. The morphology and size of the grains in this sample are similar to those of the 14Y ODS sample: equiaxed grains with small and large sizes. The grain boundaries of some submicron-sized grains are not clearly observed because of the high density of dislocations. Like the microstructures of the 14Y and 14YAl ODS samples, that of the 14YTi sample shows bimodal character. A bimodal structure is also observed for the 14YTi ODS steel, as shown in Fig. 3(c). From a comparison of the microstructures of these three ODS samples, we infer that the addition of Al or Ti does not obviously affect the microstructure of the 14Y ODS sample.

Figs. 4(a)–4(c) illustrate the grain size distribution of the

14Y, 14YAl, and 14YTi ODS steels, respectively. All of these ODS steels clearly possess bimodal structures. Both submicron-sized and micron-sized grains exist in their microstructures. The grain size of 14YAl is larger than that of 14Y and 14YTi. Overall, the 14YTi sample possesses the smallest grains. The differences in grains is attributed to the compositional disparity, and such differences in grain size will affect the performance of ODS steels.

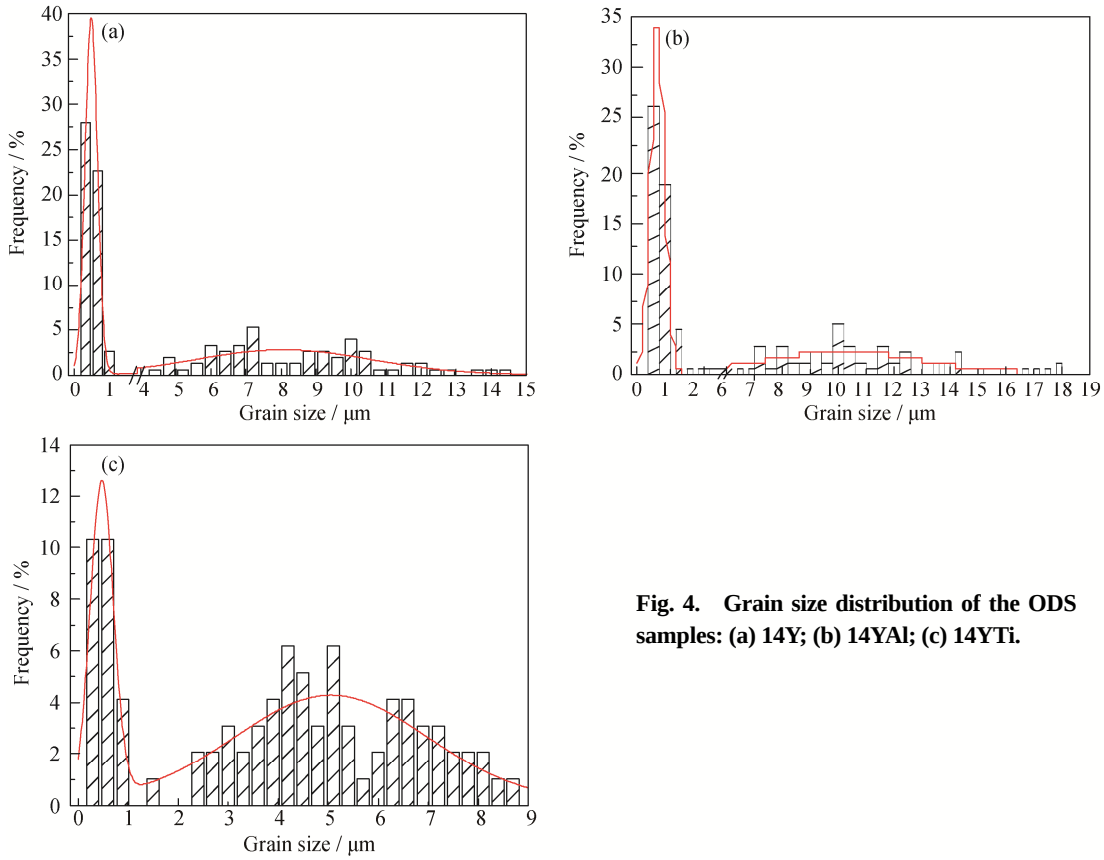

Fig. 4. Grain size distribution of the ODS samples: (a) 14Y; (b) 14YAl; (c) 14YTi.

3.2. Relative density and Vickers hardness

Fig. 5 displays the relative densities and Vickers hardnesses of the ODS samples. The relative densities of 14Y, 14YAl, and 14YTi are 98.1 ± 0.3%, 98.3 ± 0.5%, and 98.1 ± 0.2%, respectively. All the ODS samples exhibit a high density, indicating that the sintering effectively consolidated the as-milled powders. The relative densities of the ODS samples were calculated as the ratio of the measured density to the theoretical density. The theoretical densities were calculated according to the formula in Ref. [26]. The load applied during the measurement of the Vickers hardness was 50 g, and the Vickers hardness of 14Y, 14YAl, and 14YTi were 354 ± 10, 330 ± 5, and 377 ± 12, respectively. In general, obvious differences between the microhardness of the ODS samples are evident in Fig. 5. The microhardness of 14YAl is lower than that of 14Y because of the addition of Al. As demonstrated in recent years, the presence of Al in ODS steels plays a key role in improving the ductility, and the strength of ODS steels containing Al is inferior to that of

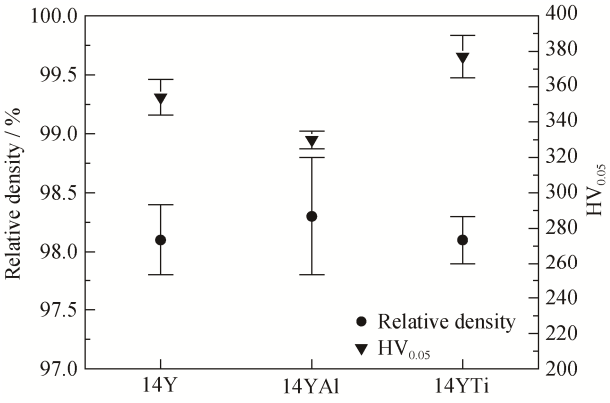

Fig. 5. Relative density and Vickers hardness results for ODS steels.

ODS steels without Al [25]. This difference may be the main reason for the lower microhardness of 14YAl compared with that of 14Y. In addition, according to the grain-refinement strengthening effect and the grain size distribution results, the large grain size of 14YAl also contri-

butes to its low hardness. The 14YTi sample clearly exhibits the highest microhardness among the three ODS samples, implying that the addition of Ti tends to increase the strength. Microhardness differences among the ODS samples show the various effects of the alloying elements. Al and Ti powders introduced into the ODS samples have opposite effects on the microhardness. Such a phenomenon is attributed to the nanoparticles in the ODS steels, which are analyzed in the next section.

3.3. Nanoparticles

The distribution of nanoparticles precipitated near the grain boundaries of large grains is shown in Fig. 6. Fig. 6(a) shows the homogeneously distributed nanoparticles in the 14Y ODS sample. The sizes of the nanoparticles range from 20 to 50 nm. All of the nanoparticles are Y_2O_3 because no other elements were added to the 14Y ODS sample. As illustrated in Fig. 6(b), nanoparticles distributed near the boundaries of large grains are also observed in the 14YAl ODS sample, and the size of these particles is similar to that of the particles in the 14Y ODS sample. However, the nanoparticles are mainly Y–Al–O nanoparticles rather than Y_2O_3. The addition of Al promotes the formation of Y–Al–O nanoparticles, and their formation mechanism has been investigated in a previous study [8]. No nanoparticles are observed in Fig. 6(c) because the Y–Ti–O nanoparticles precipitated along the boundaries of large grains in the 14YTi ODS sample are much smaller than the nanoparticles precipitated along the boundaries of large grains in the 14Y and 14YAl ODS samples. Capdevila *et al.* [23] have found that coarsening of the nanoparticles distributed on and near the grain boundaries is much easier than that of the nanoparticles distributed in the interior of grains even though no obvious difference in composition or crystal structure is observed. No similar results related to Y–Ti–O nanoparticles have been reported thus far. From this perspective, the addition of Ti, not Al, is more effective for preventing the coarsening of nanoparticles in ODS steels.

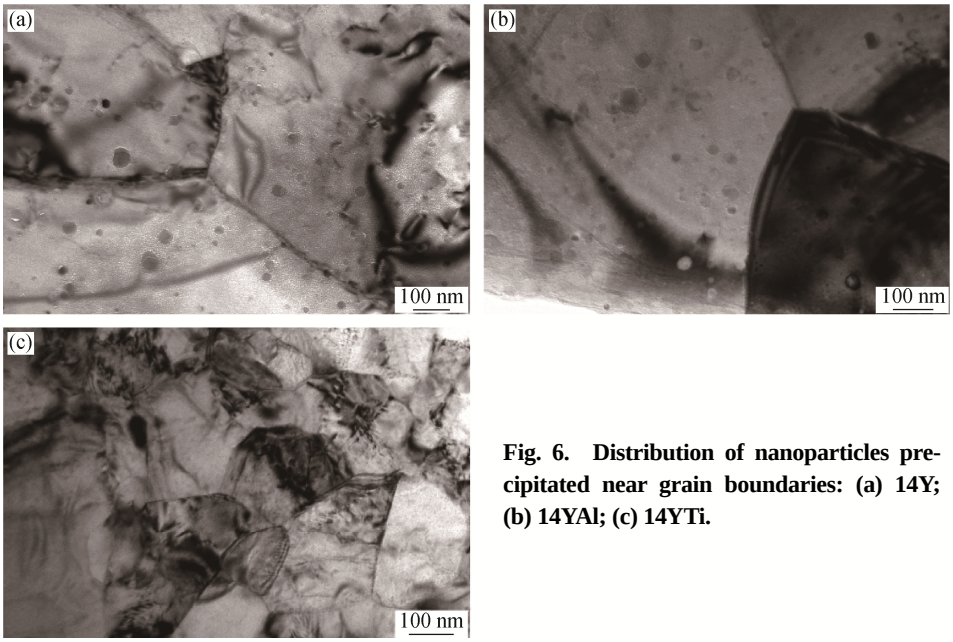

Fig. 6. Distribution of nanoparticles precipitated near grain boundaries: (a) 14Y; (b) 14YAl; (c) 14YTi.

The spatial distribution of nanoparticles precipitated in the interior of grains in the ODS samples is illustrated in Fig. 7. Figs. 7(a)–7(c) show the spatial distribution of nanoparticles in the 14Y, 14YAl, and 14YTi ODS samples, respectively. The oxide particles in the 14YAl ODS sample are smaller than those in the 14Y ODS sample, and the same phenomenon is observed in the 14YTi ODS sample. In addition, particles in the 14YTi ODS sample exhibit the smallest size compared with the particles in the other two samples. The Y–Al–O nanoparticles in the interior of grains are smaller than the nanoparticles distributed near the boundaries of large grains. However, the average size of the Y–Ti–O nanoparticles is approximately 5 nm, which is much smaller than that of the Y–Al–O nanoparticles. We concluded that the size of particles is efficiently reduced by introducing Al and Ti powders and that the refining effect of Ti is more remarkable than that of Al. Smaller nanoparticles result in a greater pinning effect, which results in better mechanical performance [9–10]. Therefore, the addition of Ti is more effective than the addition of Al for improving the pinning effect.

Fig. 8 depicts the size distribution of the nanoparticles in the ODS samples. In general, Al and Ti in the ODS samples

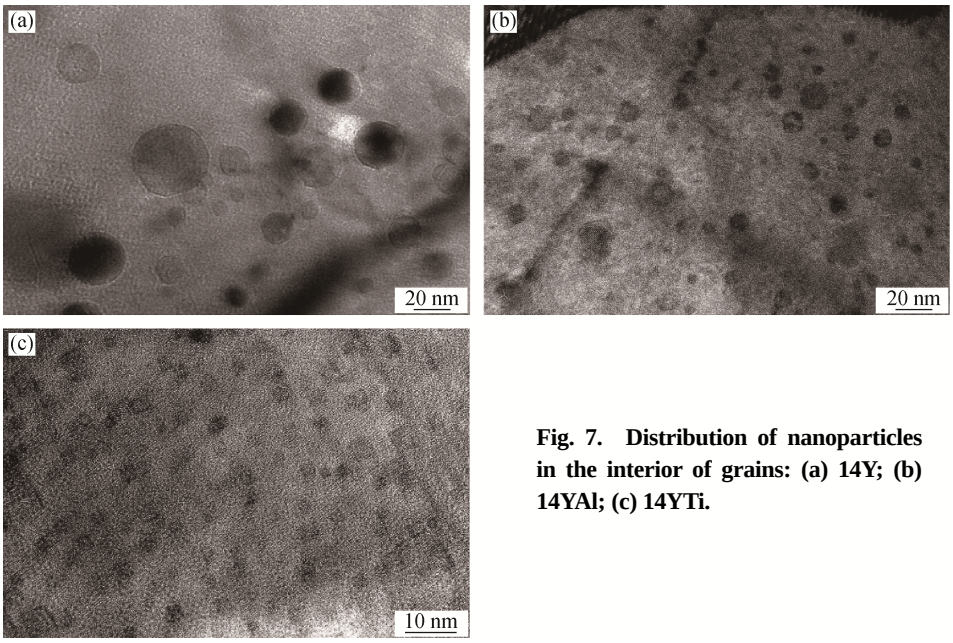

Fig. 7. Distribution of nanoparticles in the interior of grains: (a) 14Y; (b) 14YAl; (c) 14YTi.

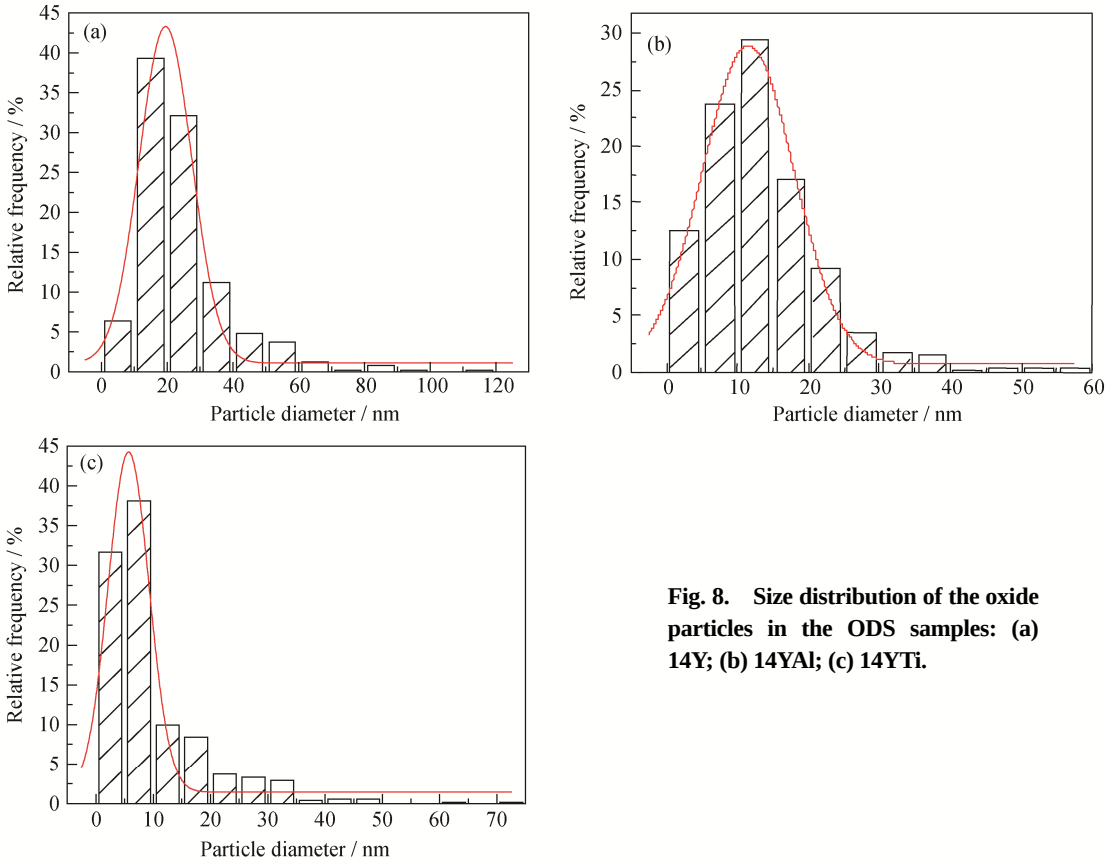

Fig. 8. Size distribution of the oxide particles in the ODS samples: (a) 14Y; (b) 14YAl; (c) 14YTi.

refine the particle size by forming Y–Al–O and Y–Ti–O particles. Most of the nanoparticles in the 14Y ODS sample are within the size range from 10 to 30 nm, as shown in Fig. 8(a), whereas most of the nanoparticles in the 14YAl ODS sample range from 5 to 15 nm (Fig. 8(b)). In Fig. 8(c), a majority of the Y–Ti–O nanoparticles in the 14YTi ODS steel are less than 10 nm in size. The particle size differences among 14Y, 14YAl, and 14YTi are likely due to the

compositional differences of their nanoparticles. The nanoparticles in 14Y, 14YAl, and 14YTi are mainly Y_2O_3, Y–Ti–O, and Y–Al–O, respectively. Many researchers have concluded that the Y–Ti–O and Y–Al–O nanoparticles are smaller than the Y_2O_3 nanoparticles in ODS steels. Some of the Y_2O_3 particles, as the originally added oxide particles, decompose into Y and O and dissolve into ferritic steels during the mechanical alloying process. The dissolved Y and O combine with Al and Ti during the consolidation process of 14YAl and 14YTi, and small-sized Y–Ti–O and Y–Al–O nanoparticles subsequently form. The spatial and size distributions of these nanoparticles correspond to the microstructure of the ODS samples. The bimodal microstructure of the ODS samples is mainly due to the grain size disparity of the pre-alloyed powders.

Fig. 9 displays a HRTEM micrograph and the corresponding fast Fourier transform (FFT) pattern of a Y_2O_3 particle with a size of approximately 20 nm in the 14Y ODS sample. The Y_2O_3 particle possesses a spherical morphology, consistent with the aforementioned TEM results. According to the identified FFT result, the Y_2O_3 particle has a body-centered cubic (bcc) crystal structure. The Y_2O_3 particle is oriented with its $1\bar{5}4$ zone axis parallel to the electron beam. All of the identified Y_2O_3 particles have a bcc crystal structure and present a spherical morphology, and these particles are the main strengthening phase in the 14Y ODS sample.

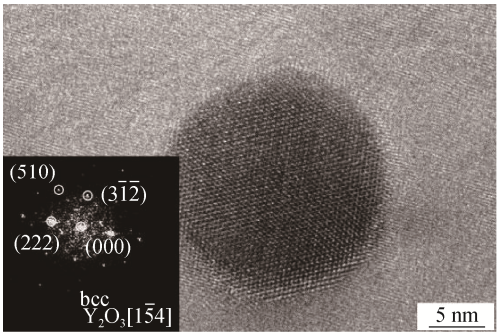

Fig. 9. HRTEM image and the corresponding fast Fourier transform pattern of a Y_2O_3 particle in the 14Y ODS steel.

Fig. 10 depicts the HRTEM micrographs and the corresponding FFT patterns of Y–Al–O particles in the 14YAl ODS sample. Fig. 10(a) gives the HRTEM image and the corresponding FFT pattern of a $YAlO_3$ particle. According to the FFT result, the $YAlO_3$ particle possesses a bcc crystal structure and is oriented with its [001] zone axis parallel to the electron beam. The $YAlO_3$ particle has a spherical morphology, and its size is approximately 20 nm. As evident in Fig. 10(b), the $Y_3Al_5O_{12}$ particle with a bcc structure also shows a spherical morphology, and it is approximately 10 nm in size. The $Y_3Al_5O_{12}$ particle is also oriented with its [001] zone axis parallel to the beam. The Y–Al–O particles may form via the reaction between Y_2O_3 and Al or via the reaction between Y_2O_3 and Al_2O_3 during the mechanical alloying and the subsequent consolidation process [8,23,31].

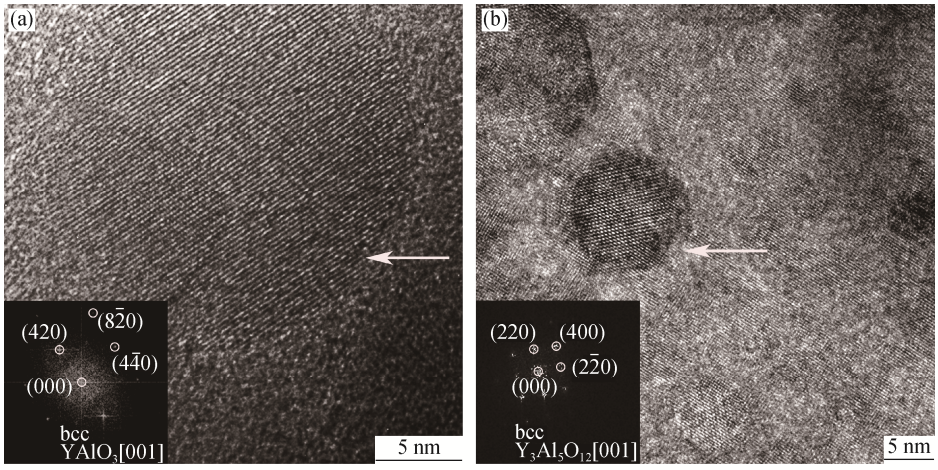

Fig. 10. HRTEM images and the corresponding fast Fourier transform patterns of (a) $YAlO_3$ and (b) $Y_3Al_5O_{12}$ in the 14YAl ODS steel.

The HRTEM micrographs and the corresponding FFT patterns of $Y_2Ti_2O_7$ particles in the 14YTi ODS sample are shown in Fig. 11. Fig. 11(a) shows a $Y_2Ti_2O_7$ particle with a spheroidal morphology, and the inset image is the corresponding FFT pattern of the particle. The FFT results demonstrate that the $Y_2Ti_2O_7$ particle has a face-centered cubic (fcc) crystal structure. Similar to the particle shown in Fig. 11(a), the particle depicted in Fig. 11(b) is also identified as $Y_2Ti_2O_7$. However, this particle exhibits a square shape, whereas that in Fig. 11(a) is spheroidal. Fig. 11(c) displays

$Y_2Ti_2O_7$ particles with other morphologies. The inset FFT pattern corresponds to the particle marked by an arrow. The formation of $Y_2Ti_2O_7$ particles is ascribed to the reaction between Y_2O_3 and Ti or to the reaction between Y_2O_3 and Ti–O compounds [31]. The results indicate that the fcc $Y_2Ti_2O_7$ particles are the predominant nanoparticles in the 14YTi ODS sample. Most of the $Y_2Ti_2O_7$ particles are approximately 5 nm in size, although larger $Y_2Ti_2O_7$ particles are still present.

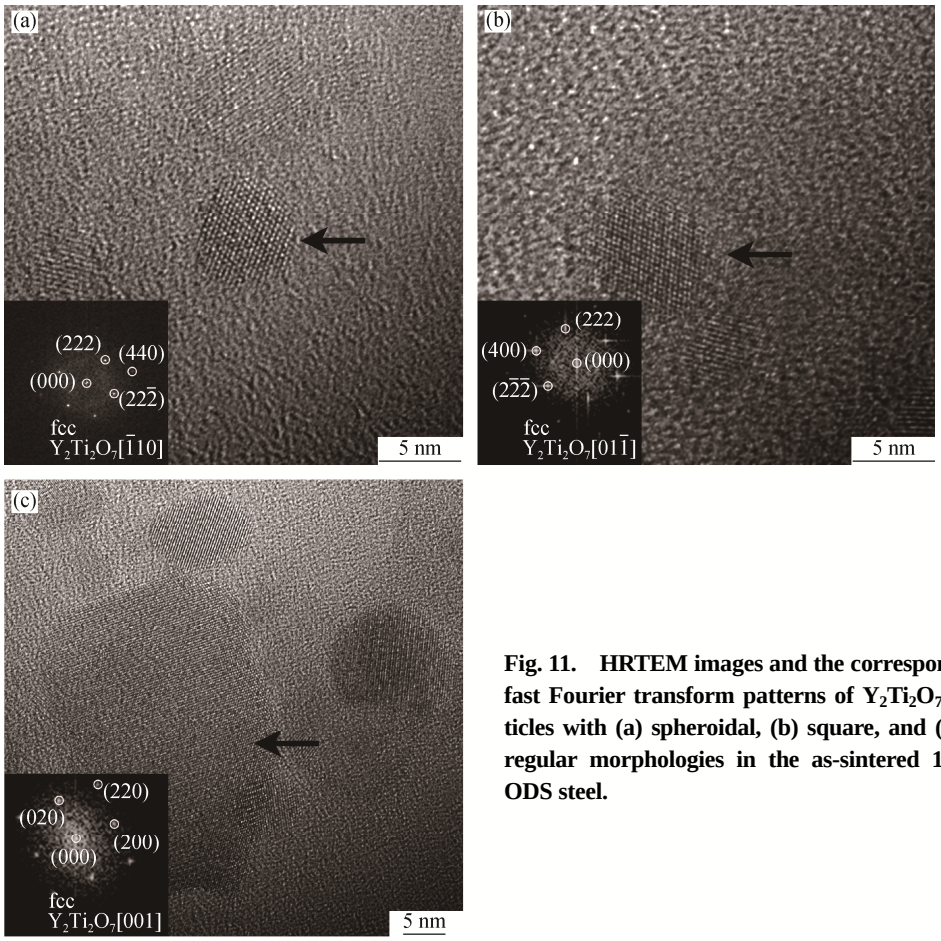

Fig. 11. HRTEM images and the corresponding fast Fourier transform patterns of $Y_2Ti_2O_7$ particles with (a) spheroidal, (b) square, and (c) irregular morphologies in the as-sintered 14YTi ODS steel.

Different alloying elements are responsible for the disparity in nanoparticles in the ODS samples. As strengthening phases, the crystal structure, stability, and the spatial and size distributions of nanoparticles in ODS samples play a key role in their final performance. Smaller nanoparticles are more efficient in hindering the movement of grain boundaries and dislocation slipping, which would result in a finer microstructure and further influence the properties of the ODS sample [7–8,32]. Understanding the respective effects of Al and Ti on the microstructure of ODS steel should facilitate the development of such structural materials.

4. Conclusions

(1) All the ODS samples possess high relative densities after HP, and the microhardness of the samples was measured and analyzed. The existence of Ti increases the hardness of the ODS sample compared with that of the 14Y ODS sample, whereas the addition of Al has the opposite effect.

(2) Both small and large grains exist in the 14Y, 14Al, and 14YTi ODS samples, showing a bimodal structure.

(3) The spatial and size distributions of nanoparticles in these ODS samples were investigated; Y_2O_3, $Y_3Al_5O_{12}$, and $Y_2Ti_2O_7$ nanoparticles were found in the 14Y, 14YAl, and 14YTi ODS samples, respectively.

(4) The addition of Ti obviously refines the size of oxide particles, and the refinement effect of Al is less remarkable than that of Ti.

Acknowledgements

This work was financially supported by the National Natural Science Foundation of China (Nos. 51474156 and

U1660201) and the National Magnetic Confinement Fusion Energy Research Project (No. 2015GB119000).

References

[1] A. Kimura, Current status of reduced-activation ferritic/martensitic steels R&D for fusion energy, *Mater. Trans.*, 46(2005), No. 3, p. 394.

[2] J.P. Wharry, M.J. Swenson, and K.H. Yano, A review of the irradiation evolution of dispersed oxide nanoparticles in the b.c.c. Fe–Cr system: Current understanding and future directions, *J. Nucl. Mater.*, 486(2017), p. 11.

[3] L. Raman, K. Gothandapani, and B.S. Murty, Austenitic oxide dispersion strengthened steels: A review, *Defence Sci. J.*, 66(2016), No. 4, p. 316.

[4] K. Verhiest, A. Almazouzi, N. De Wispelaere, R. Petrov, and S. Claessens, Development of oxides dispersion strengthened steels for high temperature nuclear reactor applications, *J. Nucl. Mater.*, 385(2009), No. 2, p. 308.

[5] G.R. Odette, M.J. Alinger, and B.D. Wirth, Recent developments in irradiation-resistant steels, *Annu. Rev. Mater. Res.*, 38(2008), p. 471.

[6] G.R. Odette, Recent progress in developing and qualifying nanostructured ferritic alloys for advanced fission and fusion applications, *JOM*, 66(2014), No. 12, p. 2427.

[7] T.K. Kim, S. Noh, S.H. Kang, J.P. Jin, H.J. Jin, K.L. Min, J. Jang, and C.K. Rhee, Current status and future prospective of advanced radiation resistant oxide dispersion strengthened steel (ARROS) development for nuclear reactor system applications, *Nucl. Eng. Technol.*, 48(2016), No. 2, p. 572.

[8] Q. Zhao, L.M. Yu, Y.C. Liu, Y. Huang, Q.Y. Guo, H.J. Li, and J.F. Wu, Evolution of Al-containing phases in ODS steel by hot pressing and annealing, *Powder Technol.*, 311(2017), p. 449.

[9] Q. Zhao, L.M. Yu, Y.C. Liu, Y. Huang, Z.Q. Ma, H.J. Li, and J.F. Wu, Microstructure and tensile properties of a 14Cr ODS ferritic steel, *Mater. Sci. Eng. A*, 680(2017), p. 347.

[10] W. Li, T. Hao, R. Gao, X.P. Wang, T. Zhang, Q.F. Fang, and C.S. Liu, The effect of Zr, Ti addition on the particle size and microstructure evolution of yttria nanoparticle in ODS steel, *Powder Technol.*, 319(2017), p. 172.

[11] P. Olier, M. Couvrat, C. Cayron, N. Lochet, and L. Chaffron, Incidence of mechanical alloying contamination on oxides and carbides formation in ODS ferritic steels, *J. Nucl. Mater.*, 442(2013), No. 1-3, Suppl. 1, p. S106.

[12] M. Magini, A. Iasonna, and F. Padella, Ball milling: An experimental support to the energy transfer evaluated by the collision model, *Scripta Mater.*, 34(1996), No. 1, p. 172.

[13] M. Nagini, R. Vijay, M. Ramakrishna, A.V. Reddy, and G. Sundararajan, Influence of the duration of high energy ball milling on the microstructure and mechanical properties of a 9Cr oxide dispersion strengthened ferritic–martensitic steel, *Mater. Sci. Eng. A*, 620(2017), p. 490.

[14] C. Suryanarayana, Mechanical alloying and milling, *Prog. Mater. Sci.*, 46(2001), No. 1-2, p. 1.

[15] I. Hilger, X. Boulnat, J. Hoffmann, C. Testani, F. Bergner, Y. De Carlan, F. Ferraro, and A. Ulbricht, Fabrication and characterization of oxide dispersion strengthened (ODS) 14Cr steels consolidated by means of hot isostatic pressing, hot extrusion and spark plasma sintering, *J. Nucl. Mater.*, 472(2017), p. 206.

[16] X.S. Zhou, C.X. Liu, L.M. Yu, Y.C. Liu, and H.J. Li, Phase transformation behavior and microstructural control of high-Cr martensitic/ferritic heat-resistant steels for power and nuclear plants: a review, *J. Mater. Sci. Technol.*, 31(2015), No. 3, p. 235.

[17] B. Mouawad, X. Boulnat, D. Fabrègue, M. Perez, and Y. de Carlan, Tailoring the microstructure and the mechanical properties of ultrafine grained high strength ferritic steels by powder metallurgy, *J. Nucl. Mater.*, 465(2015), p. 54.

[18] D.T. Hoelzer, K.A. Unocic, M.A. Sokolov, and T.S. Byun, Influence of processing on the microstructure and mechanical properties of 14YWT, *J. Nucl. Mater.*, 471(2016), p. 251.

[19] B. van der Schaaf, F. Tavassoli, C. Fazio, E. Rigal, E. Diegele, R. Lindau, and G. LeMarois, The development of EUROFER reduced activation steel, *Fusion Eng. Des.*, 69(2003), No. 1-4, p. 197.

[20] Z. Oksiuta, M. Lewandowska, P. Unifantowicz, N. Baluc, and K.J. Kurzydlowski, Influence of Y_2O_3 and Fe_2Y additions on the formation of nano-scale oxide particles and the mechanical properties of an ODS RAF steel, *Fusion Eng. Des.*, 86(2011), No. 9-11, p. 2417.

[21] A. Kimura, R. Kasada, N. Iwata, H. Kishimoto, C.H. Zhang, J. Isselin, P. Dou, J.H. Lee, N. Muthukumar, T. Okuda, M. Inoue, S. Ukai, S. Ohnuki, T. Fujisawa, and T.F. Abe, Development of Al added high-Cr ODS steels for fuel cladding of next generation nuclear systems, *J. Nucl. Mater.*, 417(2011), No. 1-3, p. 176.

[22] R. Gao, L.L. Xia, T. Zhang, X.P. Wang, Q.F. Fang, and C.S. Liu, Oxidation resistance in LBE and air and tensile properties of ODS ferritic steels containing Al/Zr elements, *J. Nucl. Mater.*, 455(2014), No. 1-3, p. 407.

[23] C. Capdevila, G. Pimentel, M.M. Aranda, R. Rementeria, K. Dawson, E. Urones-Garrote, G.J. Tatlock, and M.K. Miller, Role of Y–Al oxides during extended recovery process of a ferritic ODS alloy, *JOM*, 67(2015), No. 10, p. 2208.

[24] P. He, M. Klimenkov, R. Lindau, and A. Möslang, Characterization of precipitates in nano structured 14% Cr ODS alloys for fusion application, *J. Nucl. Mater.*, 428(2012), No. 1-3, p. 131.

[25] J. Chao, R. Rementeria, M. Aranda, C. Capdevila, and J. Gonzalezcarrasco, Comparison of ductile-to-brittle transition behavior in two similar ferritic oxide dispersion strengthened alloys, *Materials*, 9(2016), No. 8, p. 637.

[26] J.M. Torralba, L. Fuentes-Pacheco, N. García-Rodríguez, and M. Campos, Development of high performance powder metallurgy steels by high-energy milling, *Adv. Powder Technol.*, 24(2013), No. 5, p. 813.

[27] T. Liu, L.B. Wang, C.X. Wang, and H.L. Shen, Effect of Al content on the oxidation behavior of $Y_2Ti_2O_7$-dispersed Fe–14Cr ferritic alloys, *Corros. Sci.*, 104(2016), p. 17.

[28] J.S. Lee, C.H. Jang, I.S. Kim, and A. Kimura, Embrittlement and hardening during thermal aging of high Cr oxide dispersion strengthened alloys, *J. Nucl. Mater.*, 367-370(2007), p. 229.

[29] X.Y. Yuan, Z. Yang, X. Li, and L.Q. Chen, Effect of Cr on mechanical properties and corrosion behaviors of Fe–Mn–C–Al–Cr–N TWIP steels, *J. Mater. Sci. Technol.*, 33(2017), No. 12, p. 1555.

[30] S.F. Li, Z.J. Zhou, P.H. Wang, H.Y. Sun, M. Wang, and G.M. Zhang, Long-term thermal-aging stability of a 16Cr-oxide dispersion strengthened ferritic steel at 973 K, *Mater. Des.*, 90(2016), p. 318.

[31] R. Chinnappan, Thermodynamic stability of oxide phases of Fe–Cr based ODS steels via quantum mechanical calculations, *Calphad*, 45(2014), p. 188.

[32] X. Zhao, L.C. Guo, L. Zhang, T.T. Jia, C.G. Chen, J.J. Hao, H.P. Shao, Z.M. Guo, J. Luo, and J.B. Sun, Influence of nano-Al_2O_3-reinforced oxide-dispersion-strengthened Cu on the mechanical and tribological properties of Cu-based composites, *Int. J. Miner. Metall. Mater.*, 23(2016), No. 12, p. 1444.